Catalyst-on-Hotspot Nanoarchitecture: Plasmonic Focusing of Light onto Co-Photocatalyst for Efficient Light-to-Chemical Transformation

Carice Chong, Siew Kheng Boong, Tharishinny Raja Mogan, Jinn-Kye Lee, Zhi Zhong Ang, Haitao Li, Hiang Kwee Lee

C. Chong, S. K. Boong, T. Raja Mogan, J-. K. Lee, Z. Z. Ang, Prof. H. K. Lee

Division of Chemistry and Biological Chemistry, School of Chemistry, Chemical Engineering and Biotechnology

Nanyang Technological University

21 Nanyang Link, Singapore 637371.

Email: hiangkwee@ntu.edu.sg

H. Li

School of Chemistry and Chemical Engineering

Yangzhou University

Yangzhou, 225002, PR China.

Prof. H. K. Lee

Institute of Materials Research and Engineering

The Agency for Science, Technology and Research (A∗STAR)

2 Fusionopolis Way, #08-03, Innovis, 138634, Singapore.

Prof. H. K. Lee

Centre for Hydrogen Innovations

National University of Singapore

E8, 1 Engineering drive 3, 117580, Singapore.

Keywords: plasmon-mediated catalysis, photocatalyst, electromagnetic hotspot, nanoarchitecture, light-concentrating effect

Abstract

Plasmon-mediated catalysis utilizing hybrid photocatalytic ensembles promises effective light-to-chemical transformation, but current approaches suffer from weak electromagnetic field enhancements from polycrystalline and isotropic plasmonic nanoparticles as well as poor utilization of precious co-catalyst. Here, we achieve efficient plasmon-mediated catalysis by introducing a unique catalyst-on-hotspot nanoarchitecture obtained through the strategic positioning of co-photocatalyst onto plasmonic hotspots to concentrate light energy directly at the point-of-reaction. Using environmental remediation as a proof-of-concept application, our catalyst-on-hotspot design (edge-AgOcta@Cu_2O) enhances photocatalytic advanced oxidation processes to achieve superior organic-pollutant degradation at ~81% albeit having lesser Cu_2O co-photocatalyst than the fully deposited design (full-AgOcta@Cu_2O). Mass-normalized rate constants of edge-AgOcta@Cu_2O reveal up to 20-fold and 3-fold more efficient utilizations of Cu_2O and Ag nanoparticles, respectively, compared to full-AgOcta@Cu_2O and standalone catalysts. Moreover, our design also exhibits catalytic performance >4-fold better than emerging hybrid photocatalytic platforms. Mechanistic studies unveil that the light-concentrating effect facilitated by the dense electromagnetic hotspots is crucial to promote the generation and utilization of energetic photocarriers for enhanced catalysis. By enabling the plasmonic focusing of light onto co-photocatalyst at the single-particle level, our unprecedented design offers valuable insights in enhancing light-driven chemical reactions and realizing efficient energy/catalyst utilizations for diverse chemical, environmental and energy applications.

1. Introduction

Plasmonic catalysis promises efficient light-to-chemical transformations by concentrating light onto catalytic surface for facile reaction activation, even in ambient conditions.[1-4] Compared to conventional semiconductor photocatalysis, this approach employs noble metal nanocatalysts (Ag or Au) to effectively harness light energy through their strong and broadband absorption across the visible-NIR region.[5] These light-matter interactions can also be easily tuned and enhanced by manipulating the structural features of plasmonic nanoparticles (e.g., size and shape) and/or organizing them in proximity to promote inter-particle plasmonic coupling, resulting in the modulation of plasmonic catalytic activities.[6-9] Upon light excitation, the plasmonic nanoparticles undergo localized surface plasmon resonance (LSPR) which amplifies the localized electromagnetic field near the metal surfaces.[10] Subsequent plasmon decay leads to the generation of energetic charge carriers (e.g., hot electrons and hot holes) for driving target reduction-oxidation (redox) reactions.[11-13] These unique phenomena/properties consequently enable diverse light-driven applications of plasmonic catalysis, including water treatment, gas-to-fuel conversions, and chemical synthesis.[14] Despite the tremendous potential, the use of neat plasmonic material suffers from low catalytic performance primarily due to the rapid relaxation of hot carriers and the resulting mismatch between the fast optical and slow chemical processes.[15]

Plasmon-mediated catalysis emerges as a promising solution to address these limitations by further integrating plasmonic materials with heterogeneous co-catalysts, such as metals or semiconductors.[16] The formation of a functional heterojunction between these materials notably plays a vital role in promoting interfacial separation of photocarriers and suppressing fast charge recombination.[17] Together with the electromagnetic field enhancement from the plasmonic nanoparticles, the prolonged photocarrier lifetime facilitated by the photocatalytic ensemble is critical in enhancing photocatalysis.[18] For instance, the incorporation of Ag nanoparticles onto TiO_2 facilitated hot electron migration from the Ag nanoparticles into the

conduction band of TiO_2.[19, 20] This intermediate energy level serves as an electron relay for efficient transfer of photocarriers to reactants for chemical reactions. This metal-semiconductor hybrid design demonstrates an improved catalytic efficiency up to 16-fold higher when compared to standalone Ag or TiO_2 nanoparticles.[21] Moreover, direct measurements of plasmon-induced hot carriers (i.e., hot electron and hole) can be achieved using photoelectrochemical approach and/or photoconductive atomic force microscopy.[22, 23] However, plasmon-mediated catalysis still faces formidable performance bottleneck and restricted practicality due to two main issues. First, current designs mainly rely on polycrystalline and isotropic plasmonic nanoparticles with weak plasmonic fields, resulting in poor catalytic activity.[24] Second, co-catalysts are usually sparsely and randomly/fully deposited onto plasmonic nanoparticles, even on plasmonic cold regions (e.g., weak field enhancement).[25] The non-selective deposition of co-catalyst consequently leads to the poor utilization of co-catalyst, rendering this design impractical especially when precious materials (e.g. platinum) are used.

Herein, we achieve efficient plasmon-mediated catalysis by introducing a catalyst-on-hotspot nanoarchitecture where semiconductor co-catalyst is strategically positioned on the electromagnetic hotspots of anisotropic plasmonic nanoparticles. Our strategy integrates two important concepts. (1) We employ shape-controlled silver nano-octahedron (AgOcta) as the plasmonic building block because of the strong electromagnetic field confinement at its vertices and edges via the lightning-rod effect. (2) Precise on-particle synthesis to selectively deposit cuprous oxide (Cu_2O) nanoparticles on AgOcta's plasmonic hotspots (e.g., vertices and edges), thereby enabling the plasmonic focusing of light onto Cu_2O photocatalysts while improving light accessibility to the plasmonic core for effective field enhancement. Our design thus aims to boost plasmon-mediated chemical reactions and realize efficient energy/materials utilizations by concentrating light onto co-catalyst at the single-particle level.

We first demonstrate three nanoparticle configurations, namely bare AgOcta, selective catalyst-on-hotspot nanoarchitecture (edge-AgOcta@Cu_2O), and AgOcta fully coated with Cu_2O nanoparticles (full-AgOcta@Cu_2O). Using environmental catalysis as a proof-of-concept, we apply these plasmonic catalysts to treat organic-polluted water by *in situ* generating active radical species using light and hydrogen peroxide. Edge-AgOcta@Cu_2O achieves the highest photocatalytic degradation efficiency of ~81% within 90 min, albeit having lesser Cu_2O than full-Cu_2O@AgOcta. Notably, the catalyst-on-hotspot design drastically boosts the mass-normalized rate constants (Cu_2O or Ag mass) compared to full-Cu_2O@AgOcta and standalone nanomaterials. This superior design consequently enables up to 20-fold and 3-fold better utilizations of Cu_2O and Ag nanoparticles, respectively, and improves catalysis by up to ~5-fold over emerging hybrid photocatalytic ensembles. Mechanistic studies highlight the importance of spatially positioning co-photocatalyst on plasmonic hotspots for enhanced photocarrier generation, and the critical role of AgOcta-Cu_2O heterojunctions in promoting photocarrier separation and utilization. Our unprecedented catalyst-on-hotspot nanoarchitecture provides valuable insights for designing next-generation photocatalytic ensembles for effective plasmon-mediated catalysis, even with minimal co-catalyst loading. Achieving efficient and resource-effective light-to-chemical transformations is crucial for practical applications in diverse environmental, energy, and chemical reactions.

2. Results and Discussion

Our catalyst-on-hotspot design incorporates Ag octahedron (AgOcta) as the plasmonic core with intense electromagnetic hotspots at its edges and vertices, as well as Cu_2O nanoparticles as a co-catalyst because of its high photocatalytic activity in the visible light region (Figure 1A). We begin by synthesizing AgOcta with well-defined octahedron morphology and broad localized surface plasmonic resonances (LSPR) across the visible spectrum via the polyol reduction method (edge length, 404 ± 9 nm; Figure 1B; Figure S1, S2A, S3A).[7, 26] Cu_2O nanoparticles are subsequently grown on AgOcta via the *in situ* reduction of Cu(II) precursor. We direct the spatial deposition of Cu_2O nanoparticles on either (1) the AgOcta's edges and vertices (edge-AgOcta@Cu_2O) or (2) over the entire AgOcta surfaces (full-AgOcta@Cu_2O) by exploiting the differences in surface energies between its vertices, edges, and faces. On one hand, the kinetic control over the *in situ* deposition process affords edge-AgOcta@Cu_2O (edge length, 459 ± 11 nm; Figure 1C; Figure S2B; S3B, S4) where Cu_2O nanoparticles (~ 28 nm) are mainly positioned on target vertices and edges of the AgOcta core. On the other hand, the use of higher precursor concentration and rapid reactant addition results in non-selective Cu_2O deposition (similar size, ~30 nm) over the entire AgOcta surfaces (i.e., include faces) to form full-AgOcta@Cu_2O (edge length, 464 ± 12 nm; Figure 1D; Figure S2C, S3C). The structural integrity of the AgOcta core is preserved for both particle configurations. Additional characterizations of the plasmonic nanoarchitectures using X-ray diffraction (XRD) and X-ray photoelectron spectroscopy (XPS) confirm the chemical identity of Cu_2O nanoparticles, as evident by the presence of characteristic XRD and Cu 2p XPS features of Cu_2O (Figure S5; S6; S7).[27] The selective deposition observed in edge-AgOcta@Cu_2O is attributed to the higher surface energies and reactivity at the {100} vertices and {110} edges compared to the relatively stable {111} faces.[28, 29]

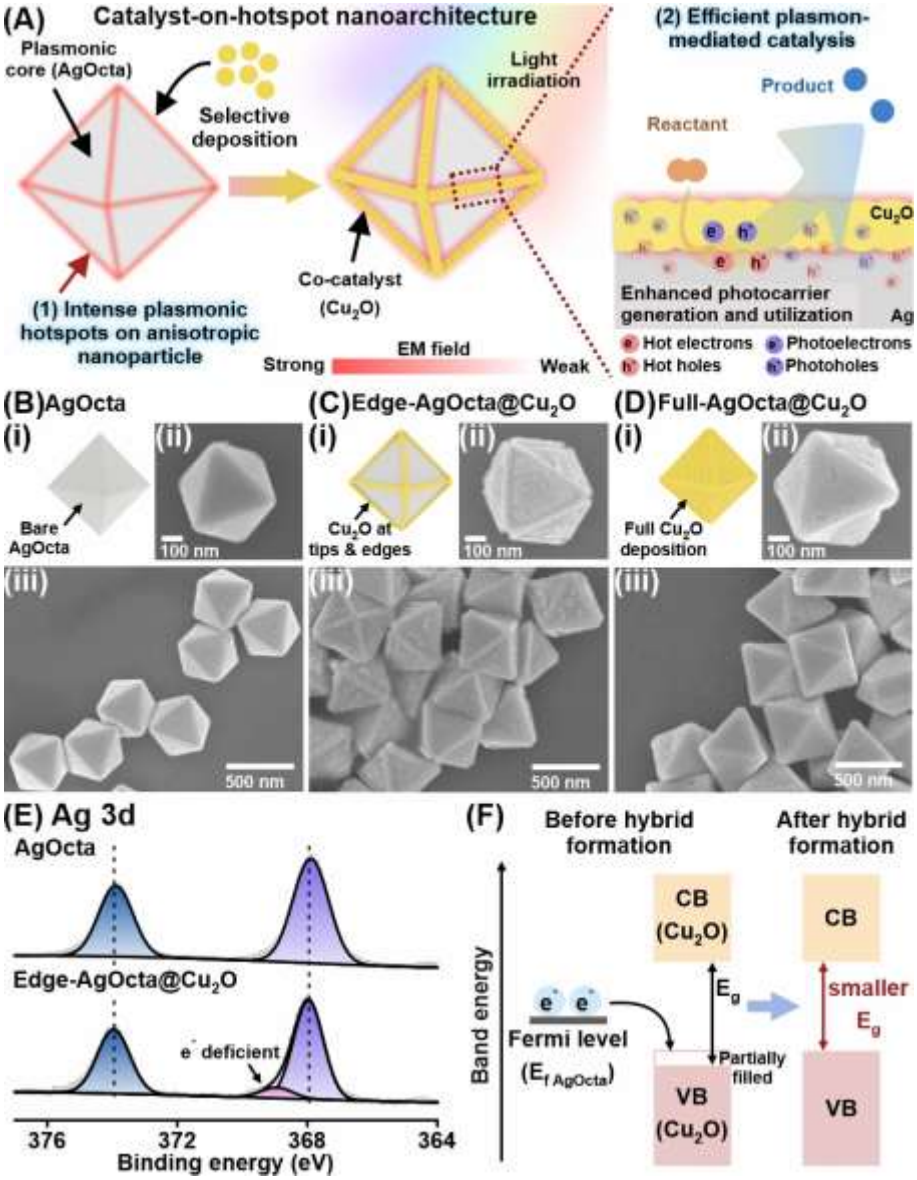

Figure 1. (A) Scheme illustrating the catalyst-on-hotspot plasmonic nanoarchitecture for efficient light-to-chemical transformation. SEM images of as-synthesized (B) AgOcta, (C) edge-AgOcta@Cu_2O, and (D) full-AgOcta@Cu_2O. (i) Schematic representation of the particle design. (ii) High and (iii) low magnification SEM images. (E) High resolution Ag 3d XPS spectra of AgOcta and edge-AgOcta@Cu_2O. (F) Band energy diagram showing the Ag-to-Cu_2O electron transfer upon the formation of the hybrid ensemble.

We further investigate the electronic interactions between the AgOcta core and Cu_2O nanoparticles in the plasmonic nanoarchitectures using XPS (Figure 1E). High resolution XPS

characterizations reveal a slight shift of the Ag 3d features to higher binding energies, indicating a decrease in the Ag's electron density after forming the hybrid ensemble. We also note the emergence of a shoulder peak at ~369 eV which is attributed to the highly electron-deficient Ag surfaces that are in direct contact with the Cu_2O nanoparticles. Moreover, the appearance of characteristic Cu 2p XPS features for both edge-AgOcta@Cu_2O and full-AgOcta@Cu_2O affirms the successful formation of Cu_2O co-catalyst (Figure S7).[30] The absence of the electron-rich peak in Cu 2p XPS spectra is because the Cu_2O involved in the Ag-Cu_2O heterojunction is hidden underneath the bulk Cu_2O nanoparticles. These observations clearly demonstrate the intimate chemical interactions between Ag and Cu_2O, as well as the electron migration from the Ag core to the partially filled valence band of Cu_2O (Figure 1F) as driven by the difference in their respective Fermi energies. Forming the Ag-Cu_2O heterojunction and promoting electron migration are crucial for facilitating photocarrier separation and enhancing electron density in the Cu_2O photocatalyst, respectively. It is worth mentioning that the electronic properties and chemical states of Ag and Cu are similar in both edge-AgOcta@Cu_2O and full-AgOcta@Cu_2O, which is a key criterion to effectively isolate the enhanced photocatalysis resulting from the nanoarchitectural design.

Understanding the structure-to-function relationships of our hierarchical designs is necessary to exemplify the importance of the strategic placement of Cu_2O photocatalyst on the intense, localized plasmonic field for effective light harvesting and utilization. Hence, we employ optical and photoelectrochemical techniques to examine the nanoarchitectures' optical properties, such as (i) plasmon resonances and Cu_2O photoabsorption, (ii) occupancy of plasmonic hotspots, and (iii) transient photocurrents. These parameters play a critical role in photocatalysis as they strongly influence light absorption, light amplification on photocatalyst, and photocarriers generation and separation, respectively. Diffuse reflectance spectroscopy (DRS) measurements of the three particle configurations demonstrate broadband light absorption in the visible-NIR region (i.e., 450 – 1000 nm; Figure 2A). The reduction of

reflectance (i.e., increase in absorption) at 400 – 600 nm in edge-AgOcta@Cu_2O and full-AgOcta@Cu_2O is due to intrinsic Cu_2O photoabsorption (Figure S8). We also observe an increase broadening of AgOcta LSPR (i.e., 600 - 1000 nm) where full-AgOcta@Cu_2O > edge-AgOcta@Cu_2O > AgOcta, possibly due to the enhanced light-matter interactions arising from extensive Ag-Cu_2O hybridization as Cu_2O coverage on AgOcta increases. To determine Cu_2O's optical bandgap, we further employ the Kubelka-Munk function (K-M function) to derive the Tauc plot from the DRS results. From the Tauc plot, standalone Cu_2O nanoparticles exhibit a direct bandgap of ~2.52 eV that matches well with reported values in the literature (Figure 2B).[31] Interestingly, the Cu_2O bandgap of edge-AgOcta@Cu_2O and full-AgOcta@Cu_2O decreases to ~2.44 eV after its deposition on AgOcta surface. This finding again supports the Ag-to-Cu_2O electron migration across the heterojunction, whereby the increase in electron density in Cu_2O's partially filled valence band reduces the energy gap between its valence and conduction bands.

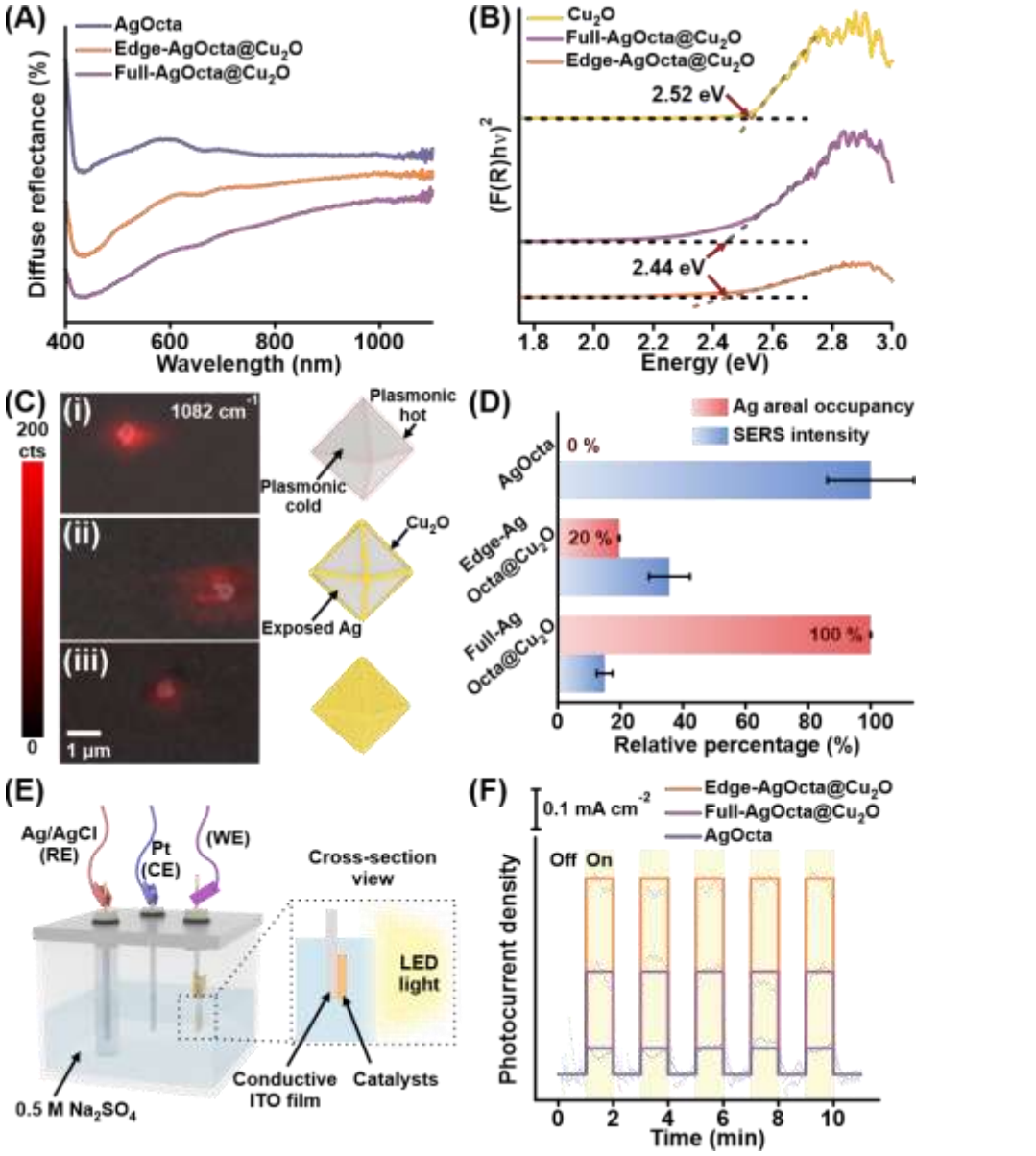

Figure 2. (A) Diffuse reflectance spectra of AgOcta, edge-AgOcta@Cu_2O, and full-AgOcta@Cu_2O. (B) Tauc plots derived from the K-M function of edge-AgOcta@Cu_2O, full-AgOcta@Cu_2O, and Cu_2O nanoparticles. (C) SERS characterizations of (i) AgOcta, (ii) edge-AgOcta@Cu_2O, and (iii) full-AgOcta@Cu_2O. Left: Overlay of SEM and SERS images of single nanoparticle. Right: Scheme illustrating the deposition of Cu_2O nanoparticles on plasmonic hot and cold regions of AgOcta. (D) Correlation of Ag areal occupancy with the observed changes in SERS intensity of 1082 cm^{-1} band across the three particle designs. (E) Scheme showing the photocurrent experimental set-up. (F) Photocurrent density of edge-

AgOcta@Cu_2O, full-AgOcta@Cu_2O, and AgOcta upon light irradiation for five successive cycles.

Next, we conduct single-particle surface-enhanced Raman scattering (SERS) experiments to assess the occupation of electromagnetic hot regions (i.e., tips and edges) on AgOcta by Cu_2O. This method ensures accurate determination of the effect of on-particle synthesis on optical properties by eliminating potential complexities arising from inter-particle plasmonic coupling. In this experiment, we first form a self-assembled monolayer of 4-methylbenzenethiol (4-MBT) as a SERS reporter on the exposed AgOcta surface and sparsely deposit these nanoparticles onto a Si wafer for SEM and SERS imaging. It is noteworthy that the occupation of Cu_2O on AgOcta's plasmonic hot areas is expected to significantly reduce SERS intensity because the 4-MBT reporters can no longer access these regions. Spatial overlapping the SEM and SERS images confirms that the SERS measurements are indeed performed on a single particle, while successful AgOcta surface functionalization is validated by the presence of 4-MBT's characteristic SERS bands at 1082 cm^{-1} (phenyl ring breathing mode and C-H in-plane bending) and 1596 cm^{-1} (phenyl stretching mode; Figure S9A).[26] Quantitative analysis of the 1082 cm^{-1} SERS feature across the three particle designs shows that AgOcta displays the highest SERS intensity of 180 ± 12 counts (Figure S9B). This is due to the absence of Cu_2O deposition (i.e., 0% areal occupancy) which allows the entire AgOcta surfaces to be grafted with the 4-MBT reporter (Figure 2C, 2D). More importantly, edge-AgOcta@Cu_2O experiences a drastic reduction in SERS intensity to ~36% of that obtained in bare AgOcta when Cu_2O is selectively deposited on the Ag tips and edges, accounting for a low 20% areal occupancy of Ag surfaces (Figure S10; Supporting information 1). Increasing areal occupancy to 100% in full-AgOcta@Cu_2O results in only a slight additional decrease in SERS intensity to ~15% of bare AgOcta's SERS intensity, signifying that the Cu_2O deposition on AgOcta's faces has minimal influence on SERS intensity. Given that the plasmonic core and Ag-MBT surface

chemistry remain consistent in the three particle designs, our findings provide compelling evidence that the plasmonic hotspots are indeed located at the AgOcta vertices and edges rather than its faces. This observation aligns with literature reporting the $>10^4$-fold stronger field enhancement on AgOcta's sharp features than its faces.[32] Achieving such precise positioning of co-catalyst on plasmonic hotspots through edge-AgOcta@Cu_2O is essential for enhancing subsequent plasmon-mediated catalysis.

The unique ability of the catalyst-on-hotspot plasmonic nanoarchitecture to enhance photocarriers generation and separation is subsequently demonstrated by comparing its transient photocurrent with control platforms, such as (i) full-AgOcta@Cu_2O, (ii) AgOcta, and (iii) Cu_2O nanoparticles. We quantify photocurrent using a photoelectrochemical setup consisting of a working electrode prepared by depositing various nanoparticles on indium tin oxide, platinum counter electrode, Ag/AgCl reference electrode, and aqueous Na_2SO_4 electrolyte (0.5 M; Figure 2E). The mass loadings of standalone Ag and Cu_2O nanoparticles are according to their respective mass compositions in edge-AgOcta@Cu_2O to ensure fair comparisons (Supporting information 2). Upon light irradiation, edge-AgOcta@Cu_2O gives the highest photocurrent density of ~0.5 mA cm^{-2} which eventually diminishes when the light is switch off (Figure 2F; Figure S11). Conversely, full-AgOcta@Cu_2O exhibits a ~50% lower photocurrent response at ~0.28 mA cm^{-2} while neat AgOcta and Cu_2O nanoparticles show the lowest photocurrent density of <0.08 mA cm^{-2}. The photocurrent responses for all three nanoparticle configurations are highly consistent with <8% deviation across five successive on-off light cycles. These comprehensive comparisons highlight three important points. (1) The strategic positioning of Cu_2O co-catalyst on plasmonic hotspots enhances the generation of photocarriers. (2) The Ag-Cu_2O hybridization creates a functional heterojunction that facilitates efficient photocarriers separation and extraction from the nanohybrid. (3) Interestingly, edge-AgOcta@Cu_2O produces a higher photocurrent response than full-AgOcta@Cu_2O, even though both designs contain Cu_2O at the plasmonic hotspots. This finding clearly underscores another

vital advantage of the catalyst-on-hotspot nanoarchitecture, particularly the reduced light shielding by the outer Cu_2O nanoparticles when positioned only at the AgOcta tips and edges. Reducing this screening effect by Cu_2O is crucial for enhancing light accessibility to the plasmonic core for effective plasmon resonances and light amplification.

As a proof-of-concept environmental application, we use the plasmonic nanoarchitectures as photocatalyst for treating organic pollutant in water using light and hydrogen peroxide (H_2O_2). Illuminating these plasmonic catalysts will induce photocatalytic advanced oxidation processes (e.g., photo-fenton process, superoxide formation), resulting in the production of highly active hydroxyl (·OH) and superoxide ($O_2{\cdot}^-$) radicals to spontaneously degrade organic pollutants (Figure 3A).[33] We select 4-nitrophenol (4-NP) as a model organic pollutant due to its severe environmental and health risks stemming from its slow natural degradation and high toxicity.[34] The reaction setup involves the deposition of plasmonic particles onto an inert polyvinylidene difluoride support (mass loading, 1.25 mg cm^{-2}), followed by its immersion in an aqueous solution containing 4-NP and H_2O_2 at a near neutral pH environment (Figure S12). We track the reaction progress by extracting reaction aliquots at predefined intervals to quantify the remaining 4-NP pollutant using its absorption peak at 317 nm and a standard calibration curve via UV-visible absorption spectroscopy (Figure S13). Upon light irradiation (e.g., white LED; Figure S14) for 90 min, edge-AgOcta@Cu_2O achieves the highest photocatalytic 4-NP degradation efficiency of 81% which is higher compared to full-AgOcta@Cu_2O (~74% efficiency) despite containing lesser Cu_2O. Bare AgOcta shows the lowest photodegradation efficiency of ~53% due to rapid hot carriers recombination in neat plasmonic material. Control experiment without photocatalyst (blank control; Figure 3B; Figure S15) exhibits negligible 4-NP degradation (≤8%), effectively ruling out potential contributions from H_2O_2 photolysis, 4-NP photobleaching, and the intrinsic reactivity between 4-NP and H_2O_2. Time-dependent reaction monitoring also unveils that 4-NP photodegradation follows a pseudo-first-order reaction kinetics described by the integrated rate law, $-\ln(C/C_0) = k_{app}t$,

where k_{app} is apparent rate constant, t is reaction duration, and C_0 and C denote 4-NP concentration at 0 min and t min, respectively. Edge-AgOcta@Cu_2O clearly exhibits the highest apparent rate constant of 0.029 min^{-1} (Figure 3C, D; Supporting Information 2), surpassing AgOcta and full-AgOcta@Cu_2O by >2.7-fold and 1.2-fold, respectively. It is also noteworthy that the trends of catalytic performance and photocurrent density are aligned (edge-AgOcta@Cu_2O > full-AgOcta@Cu_2O > AgOcta), thereby underscoring the importance of promoting photocarrier generation and utilization for enhanced photocatalysis.

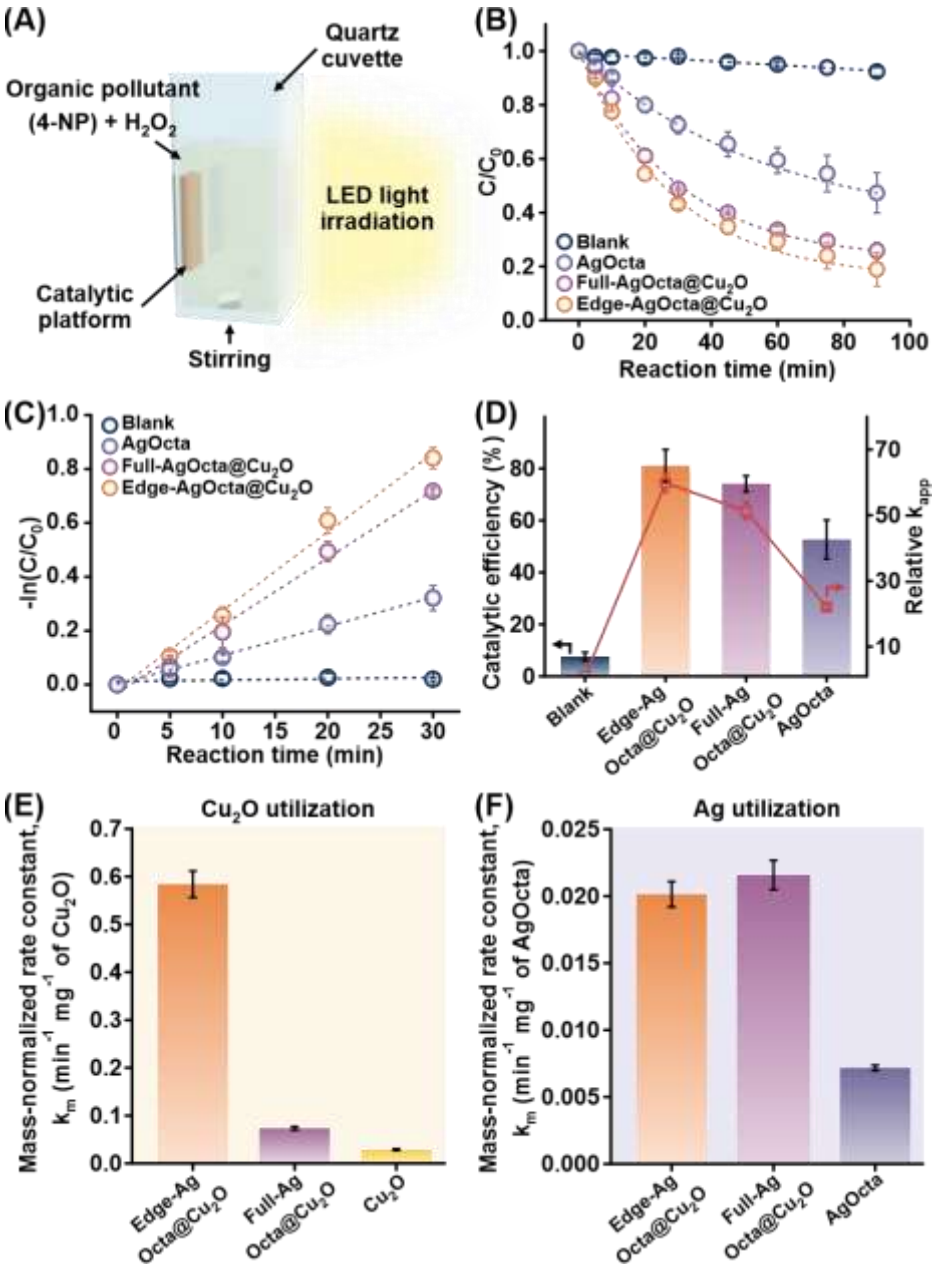

Figure 3. (A) Experimental setup for the plasmon-mediated degradation of 4-nitrophenol (4-NP). Time-dependent plots of (B) normalized 4-NP concentration (C/C_0) and (C) $-\ln(C/C_0)$ for various photocatalytic platforms. Control blank experiment (i.e., without any photocatalyst) is included for comparison. (D) Corresponding catalytic efficiencies and relative apparent rate constants (k_{app}) derived from (B) and (C), respectively. Mass-normalized rate constants (k_m) to highlight the effective utilizations of (E) Cu_2O and (F) Ag for photocatalysis via the unique catalyst-on-hotspot design.

To highlight the efficient utilization of various catalytic materials through the catalyst-on-hotspot nanoarchitecture, we normalize the reaction rate constants against the respective mass of Ag or Cu_2O present. Mass-normalized rate constant (k_m) is a widely employed parameter for fair assessment of catalytic activity between different catalysts or varying mass loadings of the same catalyst. For example, a higher mass-normalized rate constant indicates a more efficient utilization of a particular catalyst whereby smaller amount of this nanomaterial is required to achieve the same catalytic performance. Notably, the edge-AgOcta@Cu_2O possesses the highest Cu_2O-normalized rate constant of 0.584 min^{-1} mg_{Cu2O}^{-1}, which is ~8-fold and ~20-fold superior over full-AgOcta@Cu_2O and standalone Cu_2O, respectively (Figure 3E; Figure S16; Supporting information 2). When the rate constant is normalized against Ag mass, both edge-AgOcta@Cu_2O and full-AgOcta@Cu_2O demonstrate similar $k_{m, Ag}$ values of ~0.020 min^{-1} mg^{-1} that is ~3-fold higher than bare AgOcta (Figure 3F). Clearly, our unique edge-AgOcta@Cu_2O drastically enhances Cu_2O and Ag utilizations by up to 20-fold and 3-fold, respectively, in comparison to non-selective full-AgOcta@Cu_2O and standalone catalysts. This ability to achieve superior catalytic activity while using a smaller quantity of catalytic materials is a crucial attribute for practical applications. Moreover, our best-performing edge-AgOcta@Cu_2O also outperforms emerging hybrid photocatalytic systems by having up to 4.4-fold higher apparent rate constant (Table S1).[35-42] The unique advantages of edge-

AgOcta@Cu_2O arise from (1) the selective positioning of co-catalyst on plasmonic hotspots instead of plasmonic cold regions for precise plasmonic light focusing onto co-catalyst, and (2) the formation of heterojunctions to promote effective photocarriers utilization which is challenging in standalone photocatalysts.

We further investigate the underlying origins behind the exceptional photocatalytic performance of edge-AgOcta@Cu_2O by delving into the roles played by photocarrier-driven redox reactions and/or photothermal heating in the overall catalytic mechanism. We conduct additional experiments involving (i) degradation in the absence of H_2O_2 under light irradiation, (ii) degradation in the presence of H_2O_2 but in dark, and (iii) degradation in the presence of H_2O_2 in dark with heating at 45°C (Figure 4A). All control experiments employ edge-AgOcta@Cu_2O as photocatalyst and the degradation efficiency is assessed at t = 90 min. The absence of H_2O_2 results in negligible 4-NP degradation (<1%) even under identical light irradiation, underscoring H_2O_2 as a vital reactant in the photocatalytic degradation. Control dark experiments in the presence of H_2O_2 using edge-AgOcta@Cu_2O, bare AgOcta, and Cu_2O nanoparticles gives <4% 4-NP degradation, affirming that the chemical transformations are indeed initiated by light (Figure S17). More importantly, we observe that photothermal heating contributes <20% of the overall photocatalytic performance. This is evident from the ~4.5-fold lower apparent rate constant observed in the control dark experiment conducted at 45^oC (k_{app}, ~0.0065 min^{-1}) when compared to the actual plasmon-mediated photocatalysis. We choose a reaction temperature of 45^oC for comparison because it represents the maximum surface temperature recorded from the edge-AgOcta@Cu_2O under light irradiation. These systematic studies jointly highlight that the photogeneration of charge carriers (e.g., hot electrons/holes and photoelectrons/holes) and their subsequent transfer to reactant species have a major role in the superior performance of our unique catalyst-on-hotspot nanoarchitecture.

Having affirmed the photocarriers generation and transfer as the predominant energy transfer mechanism, we proceed to study the chemical process driving the H_2O_2-assisted

photocatalytic degradation of 4-NP pollutant (Figure 4B). In typical photocatalytic advanced oxidation reactions, highly energetic chemical species such as photoelectrons (e^-), photoholes (h^+), hydroxyl radical (·OH), and superoxide ion ($O_2{\cdot}^-$) could contribute to pollutant degradation. To discern the contributions of these active species, we utilize scavengers including silver nitrate ($AgNO_3$), sodium oxalate ($Na_2C_2O_4$), isopropyl alcohol (IPA), and acrylamide, respectively. It is also worth noting that a greater suppression of the catalytic reaction (i.e., lower degradation efficiency) in the presence of a specific scavenger signifies a larger contribution of the corresponding active species to the degradation process. In absence of any scavenger, the edge-AgOcta@Cu_2O displays the highest photocatalytic degradation efficiency of ~81%. Notably, the inclusion of scavengers for h^+, $O_2{\cdot}^-$, e^- and ·OH drastically diminishes catalytic efficiency to 47%, 40%, 34% and 30%, respectively. These findings unveil three vital insights into the chemical reaction pathway. First, both $O_2{\cdot}^-$ and ·OH radical species are generated *in situ* upon light radiation for pollutant degradation. Second, photogenerated holes are likely consumed by hydroxide ion and/or water to produce the hydroxyl radical due to the lower contribution of photoholes compared to ·OH radical. This observation suggests the occurrence of photo-Fenton-like reaction that also produces the ·OH radical on Cu_2O catalytic sites (to be discussed in the following paragraph). Third, the greater contribution of e^- over $O_2{\cdot}^-$ implies that photoelectrons generated by plasmonic core and Cu_2O undergo an additional utilization process besides reacting with oxygen to generate superoxide anions. This additional process is likely attributed to the utilization of photoelectrons for regenerating the Cu(I) species, again verifying the presence of photo-Fenton-like reaction.

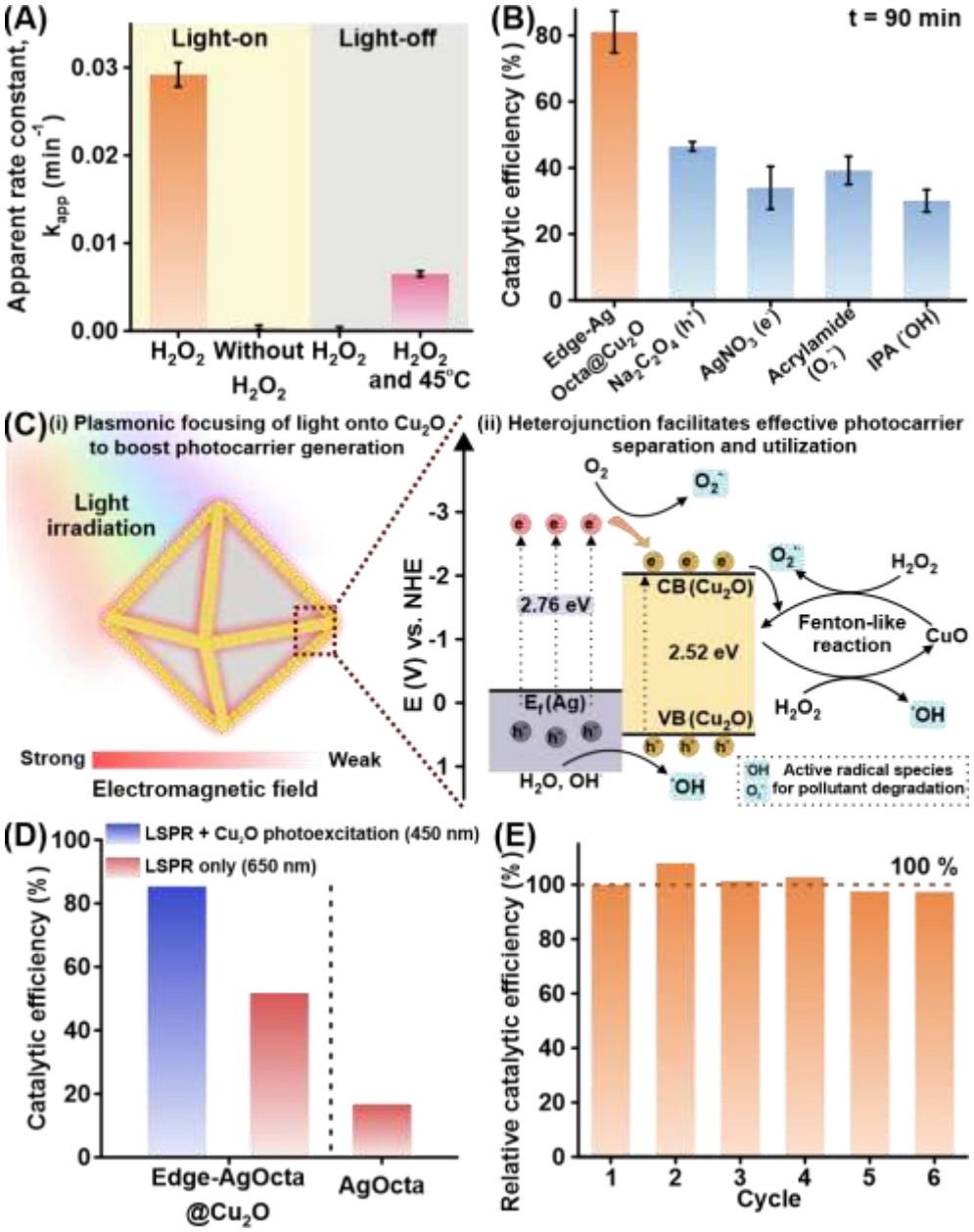

Figure 4. (A) Apparent rate constant of photocatalytic 4-NP degradation when the edge-AgOcta@Cu_2O is subjected to different reaction conditions. (B) Photocatalytic degradation efficiency of edge-AgOcta@Cu_2O when in the presence of different scavengers. (C) Proposed mechanism on the efficient photocatalytic degradation process enabled by edge-AgOcta@Cu_2O. (D) Catalytic efficiency of edge-AgOcta@Cu_2O and AgOcta upon irradiation with monochromatic light at 450 nm or 650 nm. (E) Relative catalytic efficiency of edge-AgOcta@Cu_2O over six successive photocatalytic cycles.

Together, our findings offer valuable understanding on the photocatalytic mechanism enabled by edge-AgOcta@Cu_2O at both the nanomaterial and molecular levels. Upon light excitation, the AgOcta core undergoes localized surface plasmon resonances that confine and amplify electromagnetic field at its edges and vertices (Figure 4C).[43] The non-radiative decay of plasmon leads to the generation of hot electrons and hot holes with elevated energies up to 2.76 eV (i.e., from visible light excitation) from the AgOcta's fermi level (–0.13 V vs. NHE).[44] More importantly, the strategic positioning of Cu_2O at AgOcta's tips and edges exposes the semiconductor to intense electromagnetic field, thereby enabling the plasmonic focusing of light onto the semiconductor co-catalyst to boost photoabsorption and photocarriers generation. Subsequently, the Ag-Cu_2O heterojunction facilitates the effective separation of the high density of photocarriers generated by both AgOcta and Cu_2O. For instance, the hot electrons and hot holes produced in AgOcta possess sufficient energy for their transfer to Cu_2O's conduction band (–1.96 V vs. NHE) and valence band (0.56 V vs. NHE; Figure S18), respectively.[45] The charge transfer phenomenon consequently hinders electron-hole recombination and promote the utilization of photocarriers for photoredox reactions. Photoelectrons reduce oxygen to form $O_2{\cdot}^-$ radical, while photoholes oxidize water and/or hydroxide ions into ·OH radical. Both active radical species can also be generated through a photo-Fenton-like reaction involving Cu_2O as a catalyst, whereby Cu(I)-to-Cu(II) transition promotes the formation of ·OH radical from H_2O_2 while photoelectrons facilitates the reductive regeneration of Cu(II) back to Cu(I) species.[46] The presence of photo-Fenton-like reaction is further supported by the partial surface oxidation of Cu_2O into CuO on the AgOcta (Figure S19), and by the consumption of H_2O_2 during the photocatalytic degradation. Ultimately, the active $O_2{\cdot}^-$ and ·OH radical species drive the chemical degradation of the organic pollutant for water treatment applications. Our unprecedented catalyst-on-hotspot design assumes pivotal importance in achieving efficient plasmon-mediated photocatalysis, even with minimal co-catalyst loading. This unique advantage critically addresses the performance bottleneck

associated with weak field enhancement and suboptimal catalyst utilizations often found in existing plasmonic platforms that rely on isotropic plasmonic nanoparticles and the random/full deposition of co-catalyst.

Notably, we can also activate target optical process(es) to tune and enhance photocatalytic activity by exploiting the distinct light-to-matter interactions of individual AgOcta (e.g., 450 – 1000 nm) and Cu_2O (e.g., wavelength <650 nm) components under varying monochromatic light irradiation. For example, illuminating edge-AgOcta@Cu_2O with 450 nm light enables the plasmonic nanoarchitecture to achieve high photocatalytic degradation efficiency of ~85% similar to those obtained using white LED light. This efficient photocatalytic activity arises from concurrent activation of both AgOcta's LSPR and Cu_2O photoexcitation. In contrast, changing the monochromatic light radiation to 650 nm reduces the degradation efficiency to ~49% because only AgOcta's plasmon resonances are triggered but not Cu_2O photoexcitation (Figure 4D; Figure S20). We also note the formation of AgOcta-Cu_2O heterojunction is crucial in providing an intermediate energy level that prolongs hot carriers from AgOcta for plasmon-mediated catalysis, as demonstrated by the reduced efficiency of bare AgOcta at ~17% when exposed to the same 650 nm light irradiation. These wavelength-dependent catalytic activities also align with the trend of photocurrent density observed in edge-AgOcta@Cu_2O under varying monochromatic light. Specifically, 450 nm light irradiation induces a larger photocurrent compared to 650 nm irradiation, even under similar irradiance (Figure S21). These results underscore the importance of effectively coupling AgOcta LSPR and Cu_2O photoexcitation through the unique catalyst-on-hotspot design for enhancing photocatalytic activity beyond those of individual plasmonic- or semiconductor-based photocatalysts. Our edge-AgOcta@Cu_2O exhibits remarkable robustness and is easily reusable without needing additional treatment, as evident from the consistent photocatalytic degradation efficiency (<7% deviation) over six consecutive catalytic cycles (Figure 4E; Figure

S22). Moreover, the plasmonic nanoarchitecture also maintains its distinct structural features and chemical integrity throughout repeated usage (Figure S23; S24; S25).

3. Conclusion

In conclusion, we have achieved efficient plasmon-mediated, light-to-chemical conversion by introducing a unique catalyst-on-hotspot nanoarchitecture where co-photocatalysts are strategically positioned on the intense electromagnetic hotspots of anisotropic plasmonic nanoparticle. Notably, this unprecedented design enables effective light concentration onto semiconductor photocatalyst for facile reaction activation, even with minimal co-catalyst required. As a proof-of-concept environmental application, our edge-AgOcta@Cu_2O purifies organic-polluted water at the highest efficiency of ~81% within a short reaction duration of 90 min, which is ~1.1-fold and 1.5-fold higher than full-Cu_2O@AgOcta and AgOcta, respectively. Comparisons of mass-normalized rate constants across various catalytic platforms highlights that the catalyst-on-hotspot design allows up to 20-fold and 3-fold better utilizations of Cu_2O and Ag nanoparticles, respectively, and improves catalysis by up to 4.4-fold over other emerging hybrid photocatalytic platforms. Mechanistic studies unveil the importance of the light-concentrating effect to boost photocarrier generation, and the role of AgOcta-Cu_2O hybridization to promote photocarrier separation and utilization for enhanced photocatalysis. Our on-particle design can be extended to a library of catalytic reactions by employing other plasmonic particles and/or photocatalysts as building blocks. These valuable insights create enormous opportunities towards achieving efficient plasmon-mediated catalysis in chemical synthesis, environmental remediation, and solar fuel generation.

4. Experimental Section/Methods

Chemicals: Silver nitrate (≥ 99%), polyvinylpyrrolidone (PVP, MW = 55000), anhydrous 1,5-pentanediol (PD, ≥ 97%), copper(II) chloride (97%), copper (II) sulphate (≥ 99%), sodium citrate dihydrate (≥ 99%), L-ascorbic acid (≥ 99%), 4-methylbenzenethiol (4-MBT, 98%), and 4-nitrophenol (99%) were purchased from Sigma-Aldrich; Sodium hydroxide (AR grade) was from Schedelco; Sulfuric acid (95-97%) and hydrochloric acid (37%) were from Honeywell; Ethanol (≥ 98%, AR grade) and acetone were obtained from Fischer Scientific; Hydrogen peroxide (H_2O_2, 30%) was from Scharlab. All chemicals were used without further purification. Milli-Q water (> 18.0 MΩ.cm) was purified with a Sartorius Arium 611 ® UV ultrapure water system.

Synthesis and purification of silver octahedron (AgOcta): The synthesis of AgOcta was based on the method reported in literature.[26] Briefly, polyvinylpyrrolidone (PVP; 20 mg/mL), silver nitrate (20 mg/mL), and copper (II) chloride (8 mg/mL) were added separately to 10 mL of 1,5-pentanediol (PD) through continuous vortex and sonication until fully dissolved. 35 μL copper (II) chloride solution was then added to the silver nitrate solution. 20 mL of PD in a round-bottomed flask was heated to 190 ^{o}C for 10 min. 250 μL of PVP was added to the flask dropwise every 30 s, while 500 μL silver nitrate was added one-shot every minute. The addition lasted for ~12 min to obtain Ag nanocube. The Ag nanocube was then used as seed solution for subsequent growth into Ag octahedra (AgOcta) using the same injection method with a total volume of 30 mL PVP (20 mg/mL) and 30 mL of silver nitrate (40 mg/mL) for ~ 60 min.

The purification of AgOcta started with the removal of PD by washing in acetone and ethanol through centrifugation. The resulting solution was then dispersed in 20 mL of AR ethanol and 100 mL aqueous PVP (0.2 g/L). The solution was then vacuum filtered through polyvinylidene fluoride (PVDF) filter membranes (Millipore) with pore sizes of 5000 and 650

nm and repeated several times for each pore size. The filtered AgOcta was then stored in AR ethanol and kept in fridge for further use.

Synthesis of edge Cu_2O-deposited Ag octahedron (edge-AgOcta@Cu_2O): 1.5 mL of copper(II) sulphate (1 mM) and 1 mL of sodium citrate (0.125 M) were added into 150 μL of sodium hydroxide (1 M) solution to form Cu(II)-hydroxo-citrate complex solution. In a 20 mL glass vial, ethanolic AgOcta (1 mg/mL) was added into 7.5 mL aqueous PVP solution (1mg/mL), followed by 30 μL of hydrochloric acid (2.98 M) and 750 μL of ascorbic acid (32 mM). The Cu(II)-hydroxo-citrate precursor solution was injected dropwise into the AgOcta mixture using a syringe pump at a dispensing rate of 0.65 mL/min and subsequently stirred at 750 rpm under room temperature. After the addition of Cu(II)-hydroxo-citrate precursor was completed, the reaction solution was allowed to stir for an additional 5 min. The as-fabricated edge-AgOcta@Cu_2O was then washed with copious amount of water and ethanol, and finally re-dispersed in 1 mL of ethanol.

Synthesis of full Cu_2O-deposited Ag octahedron (full-AgOcta@Cu_2O): The synthesis of full-AgOcta@Cu_2O is similar to edge-AgOcta@Cu_2O. Briefly, 1.5 mL of copper(II) sulphate (1.5 mM) and 1 mL of sodium citrate (0.125 M) were added into 150 μL of sodium hydroxide (1 M) solution to form Cu(II)-hydroxo-citrate complex solution. In a 20 mL glass vial, 750 μL of ascorbic acid (32 mM) was added into ethanolic AgOcta (1 mg/mL). The Cu(II)-hydroxo-citrate precursor solution was added one-shot to the AgOcta solution with stirring at 750 rpm under room temperature. The reaction solution was left to stir for 5 min. The as-fabricated full-AgOcta@Cu_2O was then washed with copious amount of water and ethanol, and finally re-dispersed in 1 mL of ethanol.

Synthesis of Cu_2O nanoparticles: In a 20 mL glass vial, 1 mL of sodium citrate (0.125 M), 1 mL of copper (II) sulphate (10 mM) and 500 μL of sodium hydroxide (1 M) solution were sequentially added to 7.5 mL of aqueous PVP solution (5mg/mL). The solution mixture was heated to 60 ^{o}C. 2 mL of ascorbic acid (32 mM) was added dropwise into the solution mixture and left to stir for 30 s. The reaction solution was quickly added to 15 mL of ultrapure water for centrifugation. The as-fabricated Cu_2O was then washed with copious amount of water and ethanol, and finally re-dispersed in 1 mL of ethanol/ultrapure water mixture.

Surface-enhanced Raman spectroscopy (SERS) measurement: Ethanolic solution of various nanoparticle platforms (250 μL; 4 mg/mL) was added to 750 μL of ethanol. 10 μL of ethanolic 4-methybenzenethiol (4-MBT; 10 mM) was added to the dispersion under 500 rpm stirring. After 3 h of stirring, the nanoparticles were washed with ethanol and re-dispersed in 250 μL of AR ethanol. The nanoparticles were then sparsely drop-casted onto a silicon wafer for single-particle SERS measurement.

Photocurrent evaluation of the plasmonic nanoarchitectures: The photoelectrochemical set-up comprised of sodium sulphate (0.5 M) as electrolyte solution, working electrode (area, 1 cm^2) prepared by depositing various nanoparticles on conductive indium tin oxide (ITO) substrate, a platinum wire as counter electrode, and Ag/AgCl reference electrode. The linear sweep voltammetry (LSV) was measured from 0 V to 2 V vs. Ag/AgCl reference electrode at a scan rate of 0.01 V/s. Photocurrent was measured under an applied potential of 1.8 V (vs. Ag/AgCl) under light irradiation (white LED, monochromatic 450 nm and 650nm light; 100 W) at a time interval of 0.01 s.

Preparation of the catalyst platforms for photocatalytic experiments: Ethanolic solution of various as-synthesized nanoparticles was drop-casted onto a rectangular polyvinylidene

fluoride (PVDF) membrane (pore size, 220 nm; area 1.2 cm^2) via vacuum filtration to give a uniform particle deposition. The membrane was then dried under ambient condition before further use.

Plasmon-mediated catalysis for the photodegradation of organic pollutant: As-prepared catalytic platforms (mass loading, 1.25 mg cm^{-2}) were placed in a cuvette. 3.1 mL of reactant solution comprising of equivolume of 0.2 mM 4-nitrophenol (4-NP) and 0.3 % H_2O_2 was added into the cuvette with stirring at 750 rpm. The degradation reaction was initialized by switching on the white LED light (100 W). 100 μL of aliquots were extracted at fixed time intervals and mixed with 100 μL of sulphuric acid (~ pH 3) to fully protonate the 4-NP for further characterization using UV-visible absorption spectroscopy. All reactions were repeated at least thrice to ensure the reproducibility of the results.

Quantification of 4-nitrophenol (4-NP): A standard calibration curve relating absorption intensity with 4-NP concentration was first constructed for subsequent quantification in the solution. 4-NP was first dissolved in ultrapure water and further serial-diluted to various concentrations between 5 and 160 μM. The absorption spectra were obtained using UV-visible absorption spectroscopy and the characteristic peak at 317 nm was used for further quantification.

Characterization: Scanning electron microscopy (SEM) images were captured using JEOL-JSM-7600 microscope at 5kV. Transmission electron microscopy (TEM) images were captured on a JEM-1400 (JEOL) operated at 100 kV. X-ray photoelectron spectroscopy (XPS) spectra were measured using a Phoibos 100 spectrometer with Al X-ray radiation source. All XPS spectra were calibrated against high-resolution C 1s peak at 284.5 eV. The crystal structure was obtained by powder X-ray diffraction (XRD) using a Bruker D2 Phaser diffractometer with

Cu Kα irradiation (λ = 1.54184 Å) as the incident beam at 30 kV and 10mA, scan rate at 4°/min. Diffuse reflectance spectroscopy (DRS) measurements were conducted using AvaSpec-ULS2048CL-EVO-UA-50 and an integrating sphere containing a halogen light source (AvaSphere-50-LS-HAL-12V). Single particle surface-enhanced Raman spectroscopy (SERS) measurements were performed using x-y hyperspectral imaging mode of the Ramantouch microspectrometer (Nanophoton Inc, Osaka, Japan) at an excitation wavelength of 532 nm. A 100x (N.A. 0.90) objective lens with 5 s acquisition time was used for data collection with the Raman shift ranging from 400 to 1800 cm^{-1}. Linear sweep voltammetry (LSV) and photocurrent measurements were conducted using Metrohm Autolab potentiostat. UV–visible absorption spectra were measured using an AvaSpec-ULS2048CL-EVO-UA-50 equipped with a deuterium-halogen light source (AvaLight-DH-S). A thermocouple thermometer was used to measure the temperature in the reaction setup under light irradiation.

Supporting Information

Supporting Information is available from the Wiley Online Library or from the author.

Acknowledgements

H.K.L. thanks the funding supports from the Singapore Ministry of Education (AcRF Tier 1 RS13/20 and RG4/21), A*STAR Singapore (AME YIRG A2084c0158), the National University of Singapore Center of Hydrogen Innovation (CHI-P2022-05), and the Nanyang Technological University start-up grants. The research was conducted as a part of NICES (NTU-IMRE Chemistry Lab for Eco Sustainability; REQ0275931), a joint research initiative between Nanyang Technological University (NTU) and Institute of Materials Research and Engineering (IMRE) from Agency for Science, Technology, and Research (A*STAR).

Received: ((will be filled in by the editorial staff))

Revised: ((will be filled in by the editorial staff))

Published online: ((will be filled in by the editorial staff))

References

(1) E. Cortés, L. V. Besteiro, A. Alabastri, A. Baldi, G. Tagliabue, A. Demetriadou, P. Narang *ACS Nano* **2020,** *14,* 16202.

(2) A. G. M. da Silva, T. S. Rodrigues, J. Wang, P. H. C. Camargo *Chem. Commun.* **2022,** *58,* 2055.

(3) Y. Lou, Y. Zhang, L. Cheng, J. Chen, Y. Zhao *ChemSusChem* **2018,** *11,* 1505.

(4) Y. Lou, J. He, G. Liu, S. Qi, L. Cheng, J. Chen, Y. Zhao, J.-J. Zhu *Chem. Commun.* **2018,** *54,* 6188.

(5) T. P. Araujo, J. Quiroz, E. C. M. Barbosa, P. H. C. Camargo *Current Opinion in Colloid & Interface Science* **2019,** *39,* 110.

(6) Y. H. Lee, W. Shi, H. K. Lee, R. Jiang, I. Y. Phang, Y. Cui, L. Isa, Y. Yang, J. Wang, S. Li, X. Y. Ling *Nat. Commun.* **2015,** *6,* 6990.

(7) S. K. Boong, C. Chong, J.-K. Lee, Z. Z. Ang, H. Li, H. K. Lee *Angew. Chem. Int. Ed.* **2023,** *62,* e202216562.

(8) S. Saha, J. Yang, S. S. M. Masouleh, G. A. Botton, L. Soleymani *Electrochim. Acta* **2022,** *404,* 139746.

(9) K. Song, H. Lee, M. Lee, J. Y. Park *ACS Energy Letters* **2021,** *6,* 1333.

(10) J. Li, Z. Lou, B. Li *Chin. Chem. Lett.* **2022,** *33,* 1154.

(11) S. Linic, P. Christopher, D. B. Ingram *Nature Materials* **2011,** *10,* 911.

(12) R. Verma, R. Belgamwar, V. Polshettiwar *ACS Materials Letters* **2021,** *3,* 574.

(13) A. Gellé, T. Jin, L. de la Garza, G. D. Price, L. V. Besteiro, A. Moores *Chem. Rev.* **2020,** *120,* 986.

(14) D. Wang, S. C. Pillai, S.-H. Ho, J. Zeng, Y. Li, D. D. Dionysiou *Appl. Catal., B* **2018,** *237,* 721.

(15) Y. Liu, Q. Chen, D. A. Cullen, Z. Xie, T. Lian *Nano Lett.* **2020,** *20,* 4322.

(16) C. Zhan, J. Yi, S. Hu, X.-G. Zhang, D.-Y. Wu, Z.-Q. Tian *Nature Reviews Methods Primers* **2023,** *3,* 12.

(17) Q. Li, S. Yang, R. Liu, Y. Huang, Y. Liang, C. Hu, M. Wang, Z. Liu, Y. Tai, J. Liu, Y. Li *Appl. Catal., B* **2023,** *331,* 122700.

(18) X. Chen, W. Xu, Z. Shi, Y. Ji, J. Lyu, G. Pan, J. Zhu, Y. Tian, X. Li, H. Song *Chem. Eng. J.* **2021,** *426,* 130818.

(19) J. Song, J. Long, Y. Liu, Z. Xu, A. Ge, B. D. Piercy, D. A. Cullen, I. N. Ivanov, J. R. McBride, M. D. Losego, T. Lian *ACS Photonics* **2021,** *8,* 1497.

(20) Q. Xiang, J. Yu, B. Cheng, H. C. Ong *Chemistry – An Asian Journal* **2010,** *5,* 1466.

(21) N. Pugazhenthiran, S. Murugesan, S. Anandan *J. Hazard. Mater.* **2013,** *263,* 541.

(22) J. S. DuChene, G. Tagliabue, A. J. Welch, W.-H. Cheng, H. A. Atwater *Nano Lett.* **2018,** *18,* 2545.

(23) H. Lee, H. Lee, J. Y. Park *Nano Lett.* **2019,** *19,* 891.

(24) C. Hu, X. Chen, J. Jin, Y. Han, S. Chen, H. Ju, J. Cai, Y. Qiu, C. Gao, C. Wang, Z. Qi, R. Long, L. Song, Z. Liu, Y. Xiong *J. Am. Chem. Soc.* **2019,** *141,* 7807.

(25) L. Zhou, D. F. Swearer, C. Zhang, H. Robatjazi, H. Zhao, L. Henderson, L. Dong, P. Christopher, E. A. Carter, P. Nordlander, N. J. Halas *Science* **2018,** *362,* 69.

(26) Y. Liu, S. Pedireddy, Y. H. Lee, R. S. Hegde, W. W. Tjiu, Y. Cui, X. Y. Ling *Small* **2014,** *10,* 4940.

(27) M. Mallik, S. Monia, M. Gupta, A. Ghosh, M. P. Toppo, H. Roy *J. Alloys Compd.* **2020,** *829,* 154623.

(28) A. Tao, P. Sinsermsuksakul, P. Yang *Angew. Chem. Int. Ed.* **2006,** *45,* 4597.

(29) Z. L. Wang *J. Phys. Chem. B* **2000,** *104,* 1153.

(30) G. Yang, P. Qiu, J. Xiong, X. Zhu, G. Cheng *Chin. Chem. Lett.* **2022,** *33,* 3709.

(31) L. Guo, M. Zhao, D.-M. Zhuang, M. Cao, L. Ouyang, X. Li, R. Sun, Z. Gao *Appl. Surf. Sci.* **2015,** *359,* 36.

(32) C. G. Wang, X. Z. Wu, D. Di, P. T. Dong, R. Xiao, S. Q. Wang *Nanoscale* **2016,** *8,* 4672.

(33) Y. Wang, H. Song, J. Chen, S. Chai, L. Shi, C. Chen, Y. Wang, C. He *Appl. Surf. Sci.* **2020,** *512,* 145650.

(34) N. Wang, F. Wang, F. Pan, S. Yu, D. Pan *ACS Appl. Mater. Interfaces* **2021,** *13,* 3209.

(35) K. Sahu, A. Bisht, A. Dutta, T. Som, S. Mohapatra *Surfaces and Interfaces* **2021,** *26,* 101436.

(36) L. Yang, S. Luo, Y. Li, Y. Xiao, Q. Kang, Q. Cai *Environmental Science & Technology* **2010,** *44,* 7641.

(37) S. Chu, X. Zheng, F. Kong, G. Wu, L. Luo, Y. Guo, H. Liu, Y. Wang, H. Yu, Z. Zou *Mater. Chem. Phys.* **2011,** *129,* 1184.

(38) H. Gaffour, M. Mokhtari *Res. Chem. Intermed.* **2016,** *42,* 6025.

(39) X. Liu, L. Zhao, H. Lai, S. Li, Z. Yi *Journal of Chemical Technology & Biotechnology* **2017,** *92,* 2417.

(40) A. Verma, D. P. Jaihindh, Y.-P. Fu *Dalton Transactions* **2019,** *48,* 8594.

(41) S. Padhiari, M. Tripathy, G. Hota *ACS Applied Nano Materials* **2021,** *4,* 7145.

(42) S. Mansingh, R. Acharya, S. Martha, K. M. Parida *Phys. Chem. Chem. Phys.* **2018,** *20,* 9872.

(43) D. J. Kim, S. H. Ahn, C. S. Lee, J. H. Kim *J. Mater. Chem. A* **2015,** *3,* 17644.

(44) X. Zhang, H. Sui, X. Wang, H. Su, W. Cheng, X. Wang, B. Zhao *Phys. Chem. Chem. Phys.* **2016,** *18,* 30053.

(45) M. E. Aguirre, R. Zhou, A. J. Eugene, M. I. Guzman, M. A. Grela *Appl. Catal., B* **2017,** *217,* 485.

(46) M. Fang, R. Zheng, Y. Wu, D. Yue, X. Qian, Y. Zhao, Z. Bian *Environmental Science: Nano* **2019,** *6,* 105.

The strategic positioning of semiconductor co-catalyst on the electromagnetic hotspots of anisotropic plasmonic nanoparticles is crucial to concentrate light directly at the point-of-reaction at the single-particle level. Our unique catalyst-on-hotspot design enables up to 20-fold better utilization of catalytic materials and enhances catalysis by >4-fold over emerging hybrid photocatalytic ensembles.

Carice Chong, Siew Kheng Boong, Tharishinny Raja Mogan, Jinn-Kye Lee, Zhi Zhong Ang, Haitao Li, Hiang Kwee Lee

Catalyst-on-Hotspot Nanoarchitecture: Plasmonic Focusing of Light onto Co-Photocatalyst for Efficient Light-to-Chemical Transformation